Adhesion dynamics of Janus nanocarriers to endothelial cells: A dissipative particle dynamics study

Saeed Akbarishandiz,[*] Shaghayegh Khani,[†] and Joao Maia[‡]
Department of Macromolecular Science and Engineering, Case Western Reserve University, Cleveland, Ohio 44106, USA

(Received 2 August 2023; accepted 28 March 2024; published 18 June 2024)

Janus nanocarriers (NCs) provide promising features in interfacial applications such as targeted drug delivery. Herein, we use dissipative particle dynamics simulations to study the adhesion dynamics of NCs with Janus ligand compositions to the endothelial cell as a function of a series of effects, such as the initial orientation, ligand density, shape, and size of Janus NCs. The Janus NCs, with its long axis parallel to the endothelial glycocalyx (EG) layer, has the best penetration depth due to its lower potential energy and the lowest shell entropy loss. Among different shapes of Janus NCs, both the potential energy and the EG entropy loss control the penetration. In fact, at the parallel orientations, Janus shapes with a robust mechanical strength and larger surface area at the EG/water interface can rotate and penetrate more efficiently. An increase in the ligand density of Janus NCs increases entropy losses of both the hydrophilic and the hydrophobic ligands and decreases the potential energy. Thus, for a specific Janus NCs, functionalizing with an appropriate ligand density would help driving forces prevail over barriers of penetration into the EG layer. For a particular ligand density, once the radius of the Janus NCs exceeds the appropriate size, barriers such as hydrophobic ligands and shell entropy losses are also reinforced significantly and surpass driving forces. Our observations reveal that entropy losses for hydrophobic ligands of Janus NCs and for the shell of NCs are decisive for the adhesion and penetration of Janus NCs to endothelial cells.

DOI: 10.1103/PhysRevE.109.064408

I. INTRODUCTION

Nanoscale drug delivery systems show the remarkable capability to help diagnosis and prognosis and to enhance therapeutic intervention. A few nanocarrier (NC)-based methods have been applied in clinical use; for instance, Doxil® and Abraxane® are NCs that deliver a large number of chemotherapies [1–3]. The fate of nanomaterials *in vivo* is defined by their chemical composition and physical properties, like their shape [4]. While the literature implies that asymmetric NCs with high aspect ratio can improve endothelial targeting [1,3], mainly spherical nanoparticles are used in preclinical research [5]. An important exception is the filomicelle, an asymmetric material demonstrating interesting pharmacokinetics and tumor accumulation features in drug delivery [6]. Applying functionalized NCs for targeted drug delivery demonstrates many advantages, such as enhanced efficacy and decreased toxicity, which are not seen in conventional drug delivery methods. Among accessible technologies, using precise receptor-mediated adhesion transferring of therapeutic agents to the endothelium cells results in the enhancement of specificity [7,8].

To reduce the time, effort, and cost required for developing desired NCs, computational modeling can be implemented to predict their *in vivo* behavior. Since complex drug delivery systems are rapidly developed, the integration of novel computational simulations is needed to help the study and development of NCs for diagnostics and therapeutics. For endothelial cells, a practical procedure is proposed to incorporate many of the system parameters that control the binding process, as well as the effect of the endothelial glycocalyx (EG) layer, a region outside the cell made of carbohydrates like glycoproteins and proteoglycans [8,9], on the thermodynamic impediment of nanoparticle adhesion to the cell walls.

The EG layer is well understood from the chemical composition perspective, but only some researchers explored its ultrastructure and topology [10]. The properties of the EG layer were investigated by previous simulations at the continuum level, but adequate understanding of the molecular organization still needs to be provided. In recent studies [10,11], the EG mechanics was probed using a bushlike simulation model. Kabedev and Lobaskin [10] utilized this method to explain the molecular structure of EG chains and their elastic response to indentation. Incorporating the bushlike model in their system, the authors could calculate the forces and energies needed to conquer the mechanical resistance of the EG layer. In general, there are not many studies that explore adhesion of functionalized NCs to endothelial cells with a glycocalyx layer. However, there are plenty of simulations about NC adhesion to substrate coated with polymer brushes (PBs); therefore, we provide an overview of some of these works to have some insight into the possible effect of the EG layer on adhesion of NCs. Adhesion of NCs and PBs was investigated with a variety of computational techniques [12–20]. Among them, molecular simulations [21–27] are of specific interest. These methods can directly trace nanoparticles inside PBs and calculate the change of free energy in the system.

Free energy is a critical factor for evaluating the state of a thermodynamic system. In particular, the competition between energy and entropy controls the state of a

[*]sxa641@case.edu
[†]sxk752@case.edu
[‡]Corresponding author: joao.maia@case.edu

thermodynamic system [28]. To explore the free energy of NC adhesion to PBs, Cheng *et al.* [29]. incorporated the ghost tweezer method [29,30], which is simpler than umbrella sampling [30] which requires to calculate a probability histogram to obtain the free energy profile. On the other hand, the ghost tweezer method is not capable of analyzing complex free energy profiles with numerous reaction coordinates and entirely flexible substances (like biological macromolecules). In our work the penetration of NCs into the EG layer is probed as a function of time. This goal can be achieved through studying the alteration of potential energy and entropy of the system as a function of time.

For the nanoparticle and PB the free energy of the system is influenced by the presence of the nanoparticle in the PB. The shape and size of nanoparticle and solvent-mediated interaction of the polymer and nanoparticle will determine whether the nanoparticle is repelled from or adsorbed by the PB [31]. In two different studies, self-consistent field theory (SCFT) was employed to explain the result of simulations and to evaluate the free energy of the polymer brush (ligands grafted on a nanoparticle) [32,33]. The effect of particle size on the NC's adhesion to blood vessel walls has been studied through experiment and simulation [34,35]. It was found that particles in the range 200–500 nm demonstrate weak performance in adhesion to vessel walls [34]. Also, after cell adhesion, nanosized particles show better diffusion in the cell membrane [35]. Simulation studies of spherical nanoparticles with different size and at different grafting densities of PB were done by Milchev *et al.* [36] and Merlitz *et al.* [22]. Their results demonstrated that the free energy of inclusion relates to particle radius. Not only the size but also the shape of NCs affects the adhesion. The majority of simulation works are about spherical nanoparticles in the PB [23,29,36–38]. Yet, disks and rods have been studied in some simulations and experiments [31,39,40]. One of the computational studies shows that more oblate particles show higher efficiency than spherical particles [41], while the experiment shows that disk nanoparticles have better adhesion than spheres [42]. Thus, the effect of the shape and size of NCs is still not totally clear. The energy of inclusion relates to the surface area of the nanoparticle and (for nonspherical substances) the surface-to-volume ratio. For particles that are rotationally asymmetric, it will be changed by the relative orientation of the object in the brush [13]. In a recent study [43], it was indicated that for rod-shaped particles the density of the PB defines the favorite orientation of the particle (horizontal or vertical).

Experimental groups studied different surface chemistries of functional NCs, like Janus NCs, extensively as carriers for drug delivery [44,45]. Indeed, Janus NCs, with two sides having different chemical functionalities, offer opportunities for loading multiple drugs and precisely control targeting and cargo release. Although most of the simulation works only concentrated on the adsorption of simple surface chemistry of NCs in linear PBs, a few studies investigated the variation of inclusion free energy with NC surface chemistry. In a recent simulation study [37] of adsorption of nanoparticles in brushes, the effect of Janus NCs on inclusion free energy was investigated. The results showed that it is harder for PBs to adsorb anisotropic Janus NCs than spherical Janus NCs. The authors described the observations as a rivalry between the enthalpic attraction of the polymer and the NC surface and entropic repulsion caused by polymer chains.

Tremendous advances in computational systems over the past few decades enabled computer simulation methods like molecular dynamics to contribute enormously to the study of polymeric materials at the atomic level [46]. However, these methods cannot access the time and/or length scales of macroscopic phenomena that take place in biological systems, and especially the problem investigated in this paper, which ranges approximately between 10 and 200 nm in length scale. Furthermore, implementing macroscale simulation methods will neglect the underlying physics of parameters in our complex system, such as interaction between NCs, ligands, receptors, glycocalyx chains, and endothelial cells.

In this work, Dissipative Particle Dynamics (DPD) is proposed as a mesoscale technique to overcome those drawbacks and study the dynamics of NCs near vessel wall, where the environment of endothelial cell will determine the adhesion to targeted areas.

Our previous research [47,48] delved into the targeted delivery of drugs to endothelial cells using DPD simulations. Within that study, we concentrated on analyzing how different properties of functionalized NCs affect their ability to adhere to and penetrate endothelial cells. Specifically, we investigated how NC size, shape, and ligand density impact the targeting process. Our findings highlight the crucial role of shell entropy loss in governing NC penetration. Furthermore, by examining NCs with a uniform ligand composition, we were able to overcome obstacles and explore the energetic aspects following the complete integration of NCs.

Here, we systematically study the adhesion of Janus NCs to endothelial cells under the influence of those parameters, like Janus size, shape, interfacial orientation, and surface chemistry (ligand density). To understand the adhesion process, we explore the interaction of Janus NCs and the EG layer through their potential energies and entropy losses. Our investigation of the dynamics reveals important parameters that can control the adsorption process. Our results are anticipated to be valuable in guiding the design of NCs for specific targeted drug delivery applications. Our numerical findings also elaborate on the mechanism of Janus NC penetration into the EG layer of endothelial cells.

II. METHODOLOGY

A. Simulation technique: Dissipative particle dynamics

As a particle-based simulation approach, DPD was designed to find correct hydrodynamic behavior in fluids [49]. For each particle at each time and position (r_i), the velocity (v_i) equation of motion is solved, and forces are calculated and updated at each time step. It consists of conservative ($\mathbf{F^C}$), dissipative ($\mathbf{F^D}$), and random force ($\mathbf{F^R}$) as pairwise interparticle forces. Applying these forces makes each DPD particle a frictional noisy soft sphere that interacts with other DPD spheres over time. The total force within cutoff distance which is applied by the jth neighboring particle on the ith particle is written as

$$\mathbf{F}_i = \sum_{j \neq i} \mathbf{F}^{\mathbf{C}}_{i,j} + \mathbf{F}^{\mathbf{D}}_{i,j} + \mathbf{F}^{\mathbf{R}}_{i,j}. \tag{1}$$

The conservative force $\mathbf{F^C}$ is a soft potential which is reduced linearly with respect to the center-to-center distance of two particles [Eq. (2)].

$$\mathbf{F^C_{i.j}} = a_{ij} W^C_{ij}(r_{ij}) \mathbf{e_{ij}}. \tag{2}$$

By choosing a proper repulsion coefficient between particles i and j (a_{ij}), this force can obtain equilibrium thermodynamic properties like compressibility [29]. The dissipative force $\mathbf{F^D}$ [Eq. (3)] shows viscous resistance of fluids, and its value is related to the relative velocity of the two particles and works between the center-to-center distances of particles, with the purpose of diminishing the relative velocities and kinetic energy of DPD particles:

$$\mathbf{F^D_{i.j}} = -\gamma_{ij} W^D_{ij}(r_{ij})(\mathbf{v_{ij}}.\mathbf{e_{ij}})\mathbf{e_{ij}}. \tag{3}$$

The Brownian motion in the system is represented by random force $\mathbf{F^R}$ [Eq. (4)], which, with the help of $\mathbf{F^D}$, controls the temperature of the system. A proper correlation among the values of these forces (δ_{ij}, γ_{ij}) and the weight function is required to maintain constant temperature:

$$\begin{aligned} \mathbf{F^R_{i.j}} &= \delta_{ij} W^R_{ij}(r_{ij}) \frac{\theta_{ij}}{\sqrt{\Delta t}} \mathbf{e_{ij}}, \\ \frac{\delta^2_{ij}}{2\gamma_{ij}} &= k_B T, \end{aligned} \tag{4}$$

The fluctuation-dissipation theorem [Eq. (5)] connects these forces and provides a relationship between temperature of the system and values of these forces:

$$W^D_{ij}(r_{ij}) = \left(W^R_{ij}(r_{ij})\right)^2, \tag{5}$$

Here $\boldsymbol{r_{ij}} = \boldsymbol{r_i} - \boldsymbol{r_j}$ is the vector distance between the particles, $r_{ij} = |\boldsymbol{r_{ij}}|$, and the unit vector e_{ij} is given by $\boldsymbol{e_{ij}} = \frac{\boldsymbol{r_{ij}}}{r_{ij}}$. The relative velocity of the pair of particles i and j is $\boldsymbol{v_{ij}} = \boldsymbol{v_i} - \boldsymbol{v_j}$, and θ_{ij} represents a randomly fluctuating variable with Gaussian statistics.

At distances smaller than the cutoff radius, conservative, dissipative, and random weight functions are $W^C_{ij}(r_{ij}), W^D_{ij}(r_{ij})$, and $W^R_{ij}(r_{ij})$, respectively. These weight functions have the structure $W^C_{ij}(r_{ij}) = 1 - |\boldsymbol{r_{ij}}|/r_c$, $W^D_{ij}(|\boldsymbol{r_{ij}}|) = W^R_{ij}(r_{ij})^2 = (1 - r_{ij}/r_c)^2$ at $r_{ij} < r_c$, and 0 for any $r_{ij} > r_c$. The fluctuation-dissipation theorem relates the dissipative and random weight functions, which guarantees that the momentum is conserved and hydrodynamics is preserved.

DPD simulation has been proven to serve as a successful method to study soft matter and has accurately captured the physics of Janus NCs [11,50–59].

B. Simulation setup

Following the original paper of Groot and Warren [60], the solvent-solvent repulsion parameter a_{ss} is calculated based on the dimensionless compressibility of water, k_T^{-1}; $a_{ss} = 25\ k_BT/R_c$ is obtained using a DPD system, and experimental data of water at room temperature [61]. The Neimark [29] formulation of the DPD method, which implements equal bead diameter and equal repulsion parameters for the same components, is used. According to Biagi *et al.* [61], Deng *et al.* [62], and Neimark *et al.* [29,63], the particle-particle interaction parameter is considered equal to the solvent-solvent interaction parameters ($a_{ss} = a_{PP}$) and the interaction between different beads (a_{ij}) are chosen as described below. The shell of NCs (labeled N) and ligand 1 with relatively low level of hydrophilicity have the attractive interaction of $a_{ij} = 20$ with water. Hydrophilic EG and receptor chains have the attractive interaction of $a_{ij} = 10$ with water. Hydrophilic EG and receptor chains have the attractive interaction of $a_{ij} = 5$ with shell and ligand 1 with relatively low level of hydrophilicity. The ligand-2 beads (hydrophobic) have a repulsive interaction of $a_{ij} = 30$ with EG, receptor, N, and ligand-1 beads. The "core" beads (labeled C) strongly repel all other beads in the system like water, N, and ligand-1 and ligand-2 beads with the repulsive interaction of $a_{ij} = 40$ to ensure that NCs are impenetrable.

In our simulation we use the normalized length, mass, and timescale. The cutoff radius R_c is the unit of length. The mass of solvent beads is the unit of mass m; k_BT is the unit of energy.

The microcanonical ensemble (*NVE*), which assumes constancy in the total number of particles in the system (N), the system's volume (V), and the total energy in the system (E), is utilized for DPD simulations [28,64,65] with time step $\Delta t = 0.01\tau$ with $\tau = ({}^{mR_c{}^2}/_{k_BT})^{\frac{1}{2}}$.

Accordingly, the reduced density of DPD beads, ρ^*, and the friction coefficient γ are 3 and 4.5, respectively. The solid wall is composed of three parallel layers of fixed beads. The box size is $30 \times 30 \times 60\ R_c^3$.

The EG chains are modeled as bead-spring chains with N= 20 segments for each EG filament. The harmonic spring constant is 100 and the equilibrium bond length $r_{\text{eq}} = 0.86$ are selected [62]. To mimic the molecular structure of actual EG chains and since the tethered bead of the EG chains is not free to rotate we employed EG chains with bushlike structure [10,62].

In this study, the length scales are chosen based on the macroscopic properties of the EG layer in water [8]. The physical length scale $l_{\text{phys}} = 12.5$ nm is calculated according to the experimentally obtained distance of anchor points of the glycocalyx chains, $d_{\text{phys}} = 20$ nm, and the space between anchor points of EG chains in our simulation. This choice of the physical units in our DPD simulation provides the EG thickness in the range of thicknesses for the actual EG layer (100–1000 nm) [66], thereby validating our choice of repulsion parameters and model against experimental observations.

The chain length and grafting density of ligands and receptors are obtained from experimental values [8] and are converted to the simulation scale using our physical length scale.

The EG layer and receptors are exhibited in Fig. 1. The interaction parameters and bond information for the whole endothelial system are given in Table I.

The sphere, disk, and rod shapes of nanoparticles are structured into a simple hexagonal lattice connected through harmonic bonds.

For different NC shapes, it is desirable to maintain the constant surface area instead of a constant surface area to volume ratio; first, because the surface area defines the capacity of the NC to load it with the drug, and second, at

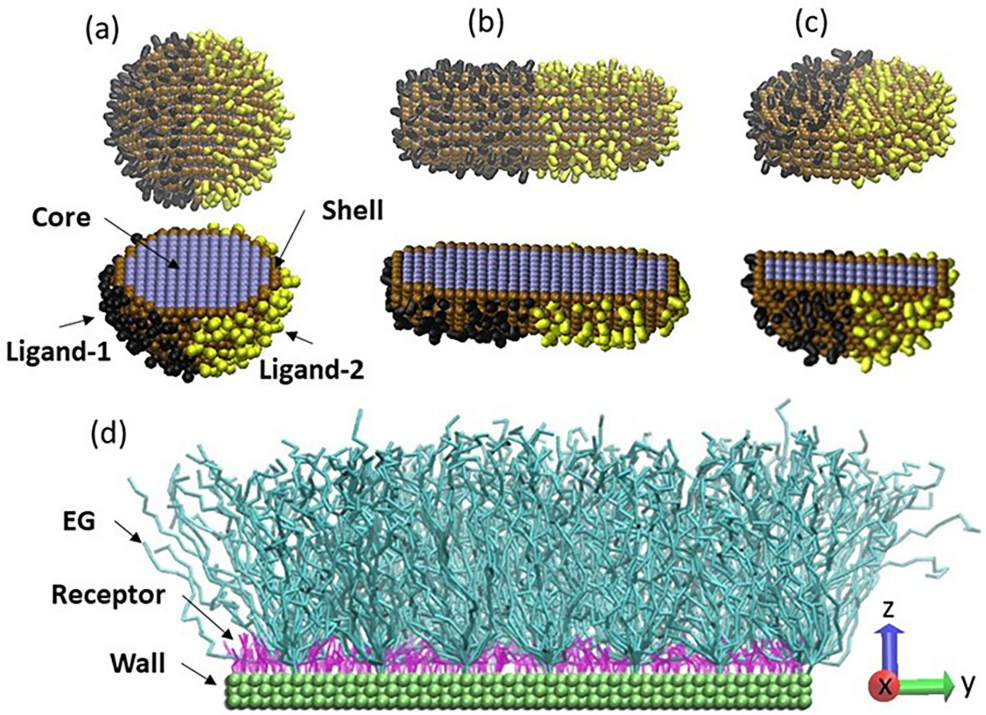

FIG. 1. Model of (a) spherical shape, (b) rod shape, (c) disk shape of Janus NCs with hydrophilic (black) and hydrophobic (yellow) ligands, shell layer (brown) and core (blue), and (d) EG chains (blue), receptors (pink), and cell wall (green). The size of the NC is $12R_c$.

a specific ligand density, it is required to have the same number of ligands on every shape of the NCs [32,67,68]. Hence, these different-shaped NCs will show equal binding strength between ligands and receptors, letting us explicitly probe the effect of shape on the adhesion of NCs to the endothelial cell. According to grafting density, ligand beads are permanently grafted at random beads on the outer layer of the NC.

Three Janus diameters—a small size of $8R_c$, medium size of $12R_c$, and large size of $16R_c$—are constructed. For other shapes of NC, three different sizes with surface areas equal to those of the sphere NCs are made. Janus NCs for sphere, disk, and rod shapes are illustrated in Fig. 1.

DPD simulations are typically carried out for 10×10^5 time steps until the system reaches the equilibrium state. To ascertain the time taken for the system to attain equilibrium, we track the temperature of the whole system until it is stabilized at 1. After 10×10^5 time steps, we detect no fluctuations in temperature, signifying that the system has reached the intended equilibrium state [60]. While the system is undergoing

TABLE I. Interaction parameters for beads in the system and chain length and bond parameters. Denotation of bead types: N is for the shell of the NC and C is for its core.

Short-range conservative repulsion

a_{ij}	EG	receptor	wall	water	C	N	lig1	lig2
EG	25.0	25.0	25.0	10.0	30.0	5.0	5.0	30.0
receptor		25.0	25.0	10.0	30.0	5.0	5.0	30.0
wall			25.0	25.0	30.0	25.0	25.0	30.0
water				25.0	40.0	20.0	20.0	40.0
C					25.0	40.0	40.0	40.0
N						25.0	25.0	30.0
lig1							25.0	30.0
lig2								25.0

Chain length and bond parameters

	kT/R_c^2	R_e/R_c		kT/R_c^2	R_e/R_c
EG_EG	100	0.86	EG_wall	100	0.86
NP_NP	500	0.57	ligand_ligand	100	0.57
recep_recep	100	0.86	ligand_NP	100	0.57
recep_wall	100	0.86			

equilibration, the NC is in the bulk water. Subsequently, the NC is repositioned on top of the EG layer and another 30×10^5 time steps of *NVE* simulation are done for the adhesion and penetration step. This 30×10^5 time-step simulation is enough to study the whole dynamics of the NCs in the system. All prior studies about the adhesion of ligand-functionalized NCs to endothelial cells, which considered all details of the system such as NC, ligands, receptors, the EG layer, water, and substrate, are continuum models [8,69]. Therefore, this work represents an improvement on the state of the art.

C. Potential energy and entropy calculations

Monitoring the variations of energy contributions will provide a better understanding of the underlying physics of the NC adsorption to the endothelial cell. In most energy studies of NC adhesion to PBs, using SCFT or umbrella sampling, the energy is calculated relative to the NC distance from the substrate inside the PB [29,39]. Nonetheless, in our dynamic study, the process of adhesion and penetration of NCs to the EG layer can be visualized while the system's energy change can be recorded over time. To reach this goal, we study the potential energy and entropy of the system during the diffusion process. During the absorption and penetration of NCs into the EG layer, there is a trade-off between entropy losses and potential energy. Here, the potential energy is calculated as a combination of all conservative energies in the system and, thus, is obtained as the sum of all nonbonded interactions between the NC's shell and ligands with the EG layer, water, receptors, and wall beads. These mainly attractive interactions act as a driving force for the inclusion of the NC into the EG layer. Average energies are collected at each time step. The potential energy (PE) of the system that is calculated as an integral of conservative forces is shown in Eq. (6):

$$\mathrm{PE} = \int \left(a_{ij} \left(1 - \frac{r_{ij}}{r_c} \right) r_{ij} \right) dr_{ij}. \tag{6}$$

Wang *et al.* [65] studied the time evolution of conservative energy of the system in a DPD simulation. Their results indicate that the system always maintains a thermal equilibrium due to the presence of random and dissipative forces (i.e., the thermostat).

Generally, it is simple to calculate the potential energy but evaluating entropy is computationally expensive. In spite of that, an expansion of the configurational entropy with respect to multibody correlation functions leads to a simple formulation that provides an approximate evaluation of entropy, given in Eq. (7) [70]. The second term of the expansion consists of the pair correlation function and is given by

$$S_2 = -2\pi \rho k_B \int_0^\infty [g(r)\ln g(r) - g(r) + 1] r^2 dr, \tag{7}$$

where ρ is the whole density, and the radial distribution function is $g(r)$. To identify local structures, S_2 could be used as a fingerprint if it properly applied to different atoms. The projection on atom i is obtained from the equation

$$s_s^i = -2\pi \rho k_B \int_0^{r_m} \left[g_m^i(r) \ln g_m^i(r) - g_m^i(r) + 1 \right] r^2 dr, \tag{8}$$

where g_m^i is the radial distribution function centered at the ith atom and r_m is an upper integration limit.

This entropy calculation method provides an instantaneous entropic snapshot of the system at each position within the simulation cell, allowing investigation as a function of time. In other words, this model can be used properly without prior knowledge of the physical state of the system. Consequently, it can be applied for dynamic systems where every step is not equilibrated [28,71–74].

According to Hadi *et al.* [71], the radial distribution function (RDF) in this method does not represent an ensemble average over all atoms in the system; rather, it contains configurational information only within the immediate neighborhood of a particular atom, providing local entropy. Moreover, our goal is not to obtain a precise absolute value for the entropy of the system but to detect a sharp change in configurational entropy, which is produced by the NC penetration. According to Piaggi and Parrinello [70], this entropy fingerprint can distinguish ordered structures in a complex situation. The $g(r)$ is normalized by the local density around each atom, which is helpful when dealing with inhomogeneous systems, such as those that have surfaces (e.g., the interface of EG and water, and the surfaces of NCs and ligands). Ghaffarizadeh and Wang [75] showed that total entropy is calculated as a weighted average of the component entropies. This form of entropy is decomposed by particle type and was used for soft materials [28,72].

During the adsorption and penetration process, entropy changes consist of three main parts: (1) the change in entropy due to the configurational changes of EG chains, called EG entropy; (2) the change in entropy due to the flexibility of the shell of our soft NCs, called shell entropy; and (3) the change in entropy associated with the conformational changes of ligands, called ligand entropy.

The entropy is always negative and the lower the entropy, the more ordered the environment. To have NC penetration of the endothelial glycocalyx layer, driving forces should be larger than barriers.

In the case of dynamics, for all the constructed NCs, translational motion of their center of mass is probed. For computing the translational motion of the NCs, the mean-square displacement (MSD) is calculated [Eq. (9)]:

$$\mathrm{MSD}\,(\tau) = \langle (\vec{r}(t + \Delta t) - \vec{r}(t))^2 \rangle, \tag{9}$$

where Δt is the lag time between the two positions. To study the diffusion of the NC to the EG layer, only the mean-square displacement tensor in the Z axis (Z_MSD) of NCs is computed.

III. RESULTS AND DISCUSSION

In this section, the influence of a series of factors on Janus NC adhesion and penetration into the EG layer is studied. First, the effect of the Janus NC initial orientation is investigated to find the best position of the NC on top of the EG layer for optimal penetration. Second, NCs with the best initial orientation are used to study the effect of ligand density. Third, NCs with the best ligand density are utilized to analyze the shape effect, and finally, the effect of size on the adhesion and penetration of Janus NCs to the EG layer is evaluated using the

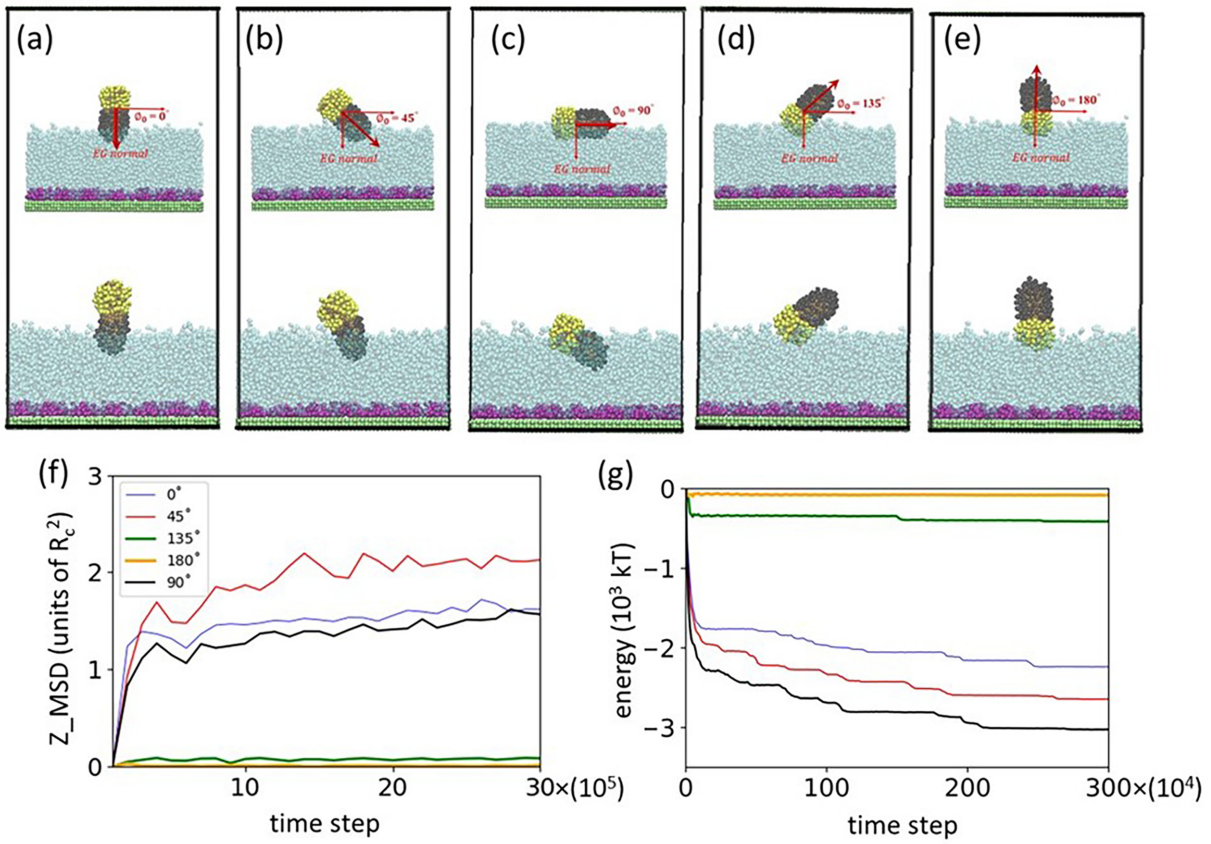

FIG. 2. VMD snapshots of (a) 0° orientation, (b) 45° orientation, (c) 90° orientation, (d) 135° orientation, and (e) 180° orientation of $8R_c$ Janus rod after 30×10^5 time steps. Inset snapshots show the initial orientation of Janus NCs at time zero. (f) Z_MSD and (g) potential energy for these NCs with different initial orientations.

best shape. The interaction between Janus NCs and EG chains during penetration is quantified through potential energy and entropy calculations.

A. Effect of initial orientation

The penetration of an NC into the EG layer is directly correlated with the initial orientation of the NC. Gao *et al.* [39] studied the effect of the NC orientation on the inclusion energy and discovered that the orientation is controlled by the adhesion energy obtained from the binding of ligands and PB, as well as the entropic loss of the PB due to the conformational hindrance imposed by the NC. To understand the effect of Janus NC orientation on its adhesion and penetration to the EG layer, we plotted the Z_MSD, potential energy, and entropy of the system as functions of NC orientation in Figs. 2 and 3.

According to the Z_MSD plot [Fig. 2(f)] and the potential energy plot [Fig. 2(g)], it is concluded that the significant difference in penetration amount between the group of 0°, 45°, and 90° orientations, and the group of 135° and 180° orientations, is determined by the significant potential energy difference between these two groups. The potential energy plot also shows that 135° and 180° orientations, with ligand 2 at the EG/water interface and ligand 1 in water, have the highest potential energy. The reason for this behavior is that ligand 1 exhibits a lower attractive interaction with water compared to its interaction with EG, and ligand 2 experiences a repulsive interaction with EG chains.

Furthermore, 135° and 180° orientations show no drop in potential energy, which indicates that they cannot penetrate into the EG layer. In contrast, among 0°, 45°, and 90° orientations, with ligand 1 located at the interface of the water and the EG layer, the 90° orientation has the highest number of ligand 1 in contact with the EG layer. As a result, initially, the 90° orientation has the lowest potential energy and the best driving force for penetration. For these orientations, the decrease in potential energy continues as the Janus NC penetrates further into the EG layer.

Entropy plots (Fig. 3) indicate that, despite the stronger attractive interaction between the NC with 90° (parallel) orientation and EG chains, its penetration with the largest surface area in contact with the EG layer results in more ordered EG chains compared to the penetration of NCs with nonparallel orientations [Fig. 3(a)]. This phenomenon occurs because the penetration of the NC with parallel orientation occupies more space between EG chains, limiting the freedom of motion for the EG chains.

The time evolution of EG entropies for the EG with NCs compared to the EG without NCs is presented in the Supplemental Material [76].

Figure S1 [76] demonstrates that the EG chains for 0°, 45°, and 90° orientations are more disordered compared to the EG without NCs. The attractive interaction between ligand 1 and

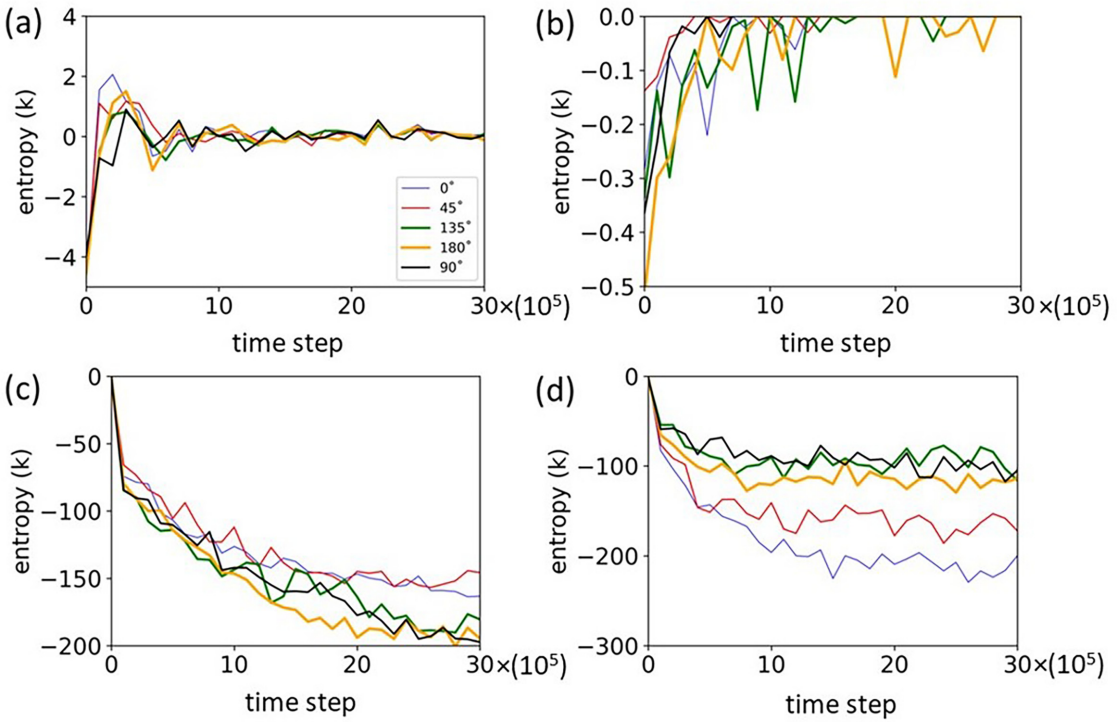

FIG. 3. Time evolution of (a) EG entropy, (b) ligand-1 entropy, (c) ligand-2 entropy, and (d) shell entropy of $8R_c$ Janus rod with different initial orientations. The blue, red, black, green, and orange (from the thinnest to the thickest) curves indicate Janus NCs with 0°, 45°, 90°, 135°, and 180° initial orientations, respectively.

EG chains allows Janus NCs of these orientations to provide EG chains with increased freedom of movement. Thus, the EG entropy serves as a strong driving force for the penetration of nonparallel orientations of Janus rods.

Furthermore, for 135° and 180° orientations, the loss of ligand-1 entropy [Fig. 3(b)] is higher, resulting in more ordered ligand-1 chains. When ligand-1 chains are in contact with water, as shown in Table I, they exhibit a lower attractive interaction compared to when they are in contact with EG chains. As a result, for the 135° and 180° orientations where ligand-1 chains are completely inside the water, they are more ordered. Conversely, for 0°, 45°, and 90° orientations, ligand-1 chains are at the interface of EG and water, leading to an attractive interaction between ligand 1 and EG chains. Consequently, at the EG/water interface, ligand-1 chains have more freedom to move and are more disordered. Therefore, ligand-1 entropy acts as a key factor influencing the penetration of different orientations of Janus rods.

Furthermore, for 0° and 45° orientations, where ligand 2 is far from the EG layer, the entropy loss of ligand-2 chains is lower, resulting in more disordered ligand-2 chains. In contrast, the other three samples, where ligand 2 is in contact with the EG layer, exhibit more ordered ligand-2 chains due to the higher repulsive interaction of EG and ligand 2, resulting in significant entropy loss. Overall, at the EG/water interface, ligand-2 chains tend to be more ordered. The slopes of ligand-1 and ligand-2 entropies also confirm that the penetration of NCs over time, which enhances the attractive ligand-1/EG interaction and the repulsive ligand-2/EG interaction, induces ligand-1 chains to be more disordered and ligand-2 chains to be more ordered.

Considering that the amount of shell entropy loss [Fig. 3(d)] is similar to the amount of ligand-2 entropy loss [Fig 3(c)] and both are two orders of magnitude larger than the amount of ligand-1 entropy loss, it is concluded that the shell entropy loss is mainly attributed to the ligand-2 entropy loss, generated by the strong repulsion of ligand 2 with EG and water. For 0° and 45° orientations, the shell becomes more ordered, while for 90°, 135°, and 180° orientations, the shell is disordered. Additionally, in these samples with different initial orientations, since the ligand-2 density is constant, the shell entropy loss is affected not only by the entropy loss of ligand 2 but also potentially reflects the direct effect of Janus orientation on the shell deformation. For 135° and 180° orientations, repulsive forces are applied to the ligand-2 side of the rod, where it is already compressed (as observed in VMD snapshots). Consequently, this side of the rod's shell cannot be ordered any further. However, for 0° and 45° orientations, the ligand-1 side stretches (as observed in VMD snapshots) due to the attractive interaction with the EG layer. Hence, one possible explanation is that their shells undergo deformation, resulting in the highest ordering. Therefore, the structural strength of the Janus shell also influences the shell entropy. The 90° orientation, with ligand 1 and ligand 2 located in the water and the EG layer, respectively, exhibits the most disordered shell. The rationale behind this is that for this orientation, attractive and repulsive forces are equal and in opposite directions, triggering a rotation of the 90° orientation rod with the lowest shell entropy loss. Moreover, due to this rotation, the ligand-2 entropy cannot significantly affect the shell entropy.

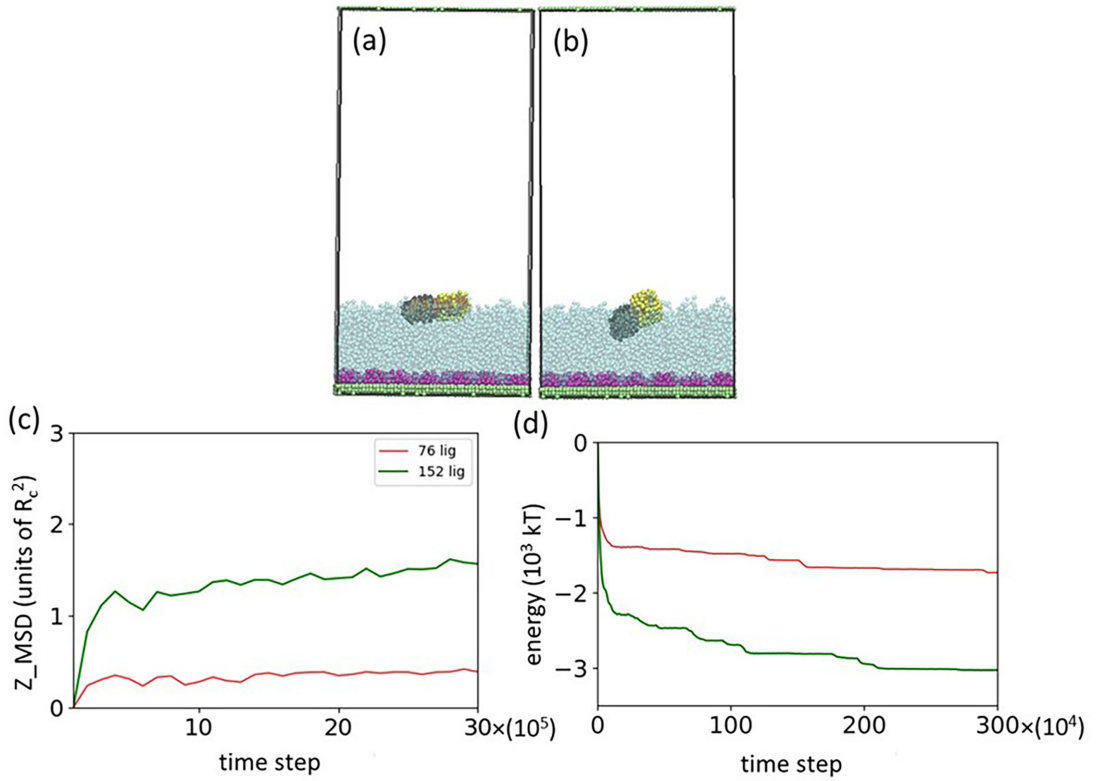

FIG. 4. VMD snapshots of (a) 76 ligands and (b) 152 ligands of $8R_c$ Janus rod after 30×10^5 time steps. (c) Z_MSD and (d) potential energy for these NCs with different ligand densities.

Comparing the 90° and 45° orientations, the former initially has a lower potential energy and lower shell entropy loss, potentially leading to fewer barriers for the penetration of Janus rods with different sizes and shapes. Furthermore, during the penetration, the 0° orientation shows a higher potential energy and a larger ligand-1 entropy loss compared to the 45° and 90° orientations, resulting in the largest shell entropy loss. Therefore, for the remaining study, the 90° or parallel orientation of Janus NCs is chosen as the initial orientation.

In general, Janus NCs exhibit different final penetration depths and energies, suggesting that the ultimate states of Janus NCs strongly depend on their initial orientations. An experimental study by Champion and Mitragotri [77] revealed that the local shape of NCs plays a crucial role in determining their diffusion rate within cells. Specifically, the orientation of NCs at the attachment point to the cell defines their local shape. Therefore, for different orientation degrees, penetration is sensitive to the initial contact between NCs and EG chains (local shape). Each individual orientation degree, characterized by the initial contact area of the hydrophobic and hydrophilic sides of the Janus NC at the EG/water interface, exhibits unique potential energy and entropies, resulting in varying penetration amounts. These observations remain consistent even within the context of 0°, 45°, and 90° orientations. Furthermore, Champion and Mitragotri [77] also discovered that a nanoparticle penetrates significantly faster through its sharp end than through its flat region. Interestingly, their findings align with our observation for the NC with a 90° orientation, which, due to its larger surface area and sharp edge at the EG/water interface, can penetrate faster than other orientations.

B. Effect of ligand density

To investigate the impact of Janus NC ligand density on the interaction with the EG layer, the potential energy and entropy for the penetration of NCs with various ligand densities into the EG layer are computed. Figures 4 and 5 illustrate the Z_MSD, potential energy, and entropy of the system as a function of the Janus ligand density.

The Z_MSD plot [Fig. 4(c)] reveals that the NC with a higher ligand density experiences a stronger driving force for penetration, resulting in longer penetration. Additionally, the potential energy plot [Fig. 4(d)] illustrates the initial binding energy, indicating that NCs with higher ligand density exhibit larger binding energy between EG ligands and lower potential energy. The steeper slope in the reduction of potential energy for Janus NCs with high ligand density indicates that a larger portion of the Janus NC is inside the EG layer, leading to more ligands binding to the EG layer. Consequently, the potential energy difference becomes a determining factor for the penetration amount.

In addition, an exploration of the impact of entropy on penetration reveals that, despite the heightened attractive interaction between the NC with 152 ligands and EG chains, its rapid penetration leads to more ordered EG chains compared to the penetration of the NC with 76 ligands [Fig. 5(a)]. This occurrence is attributed to the extensive penetration of the NC with 152 ligands, which occupies more space between EG

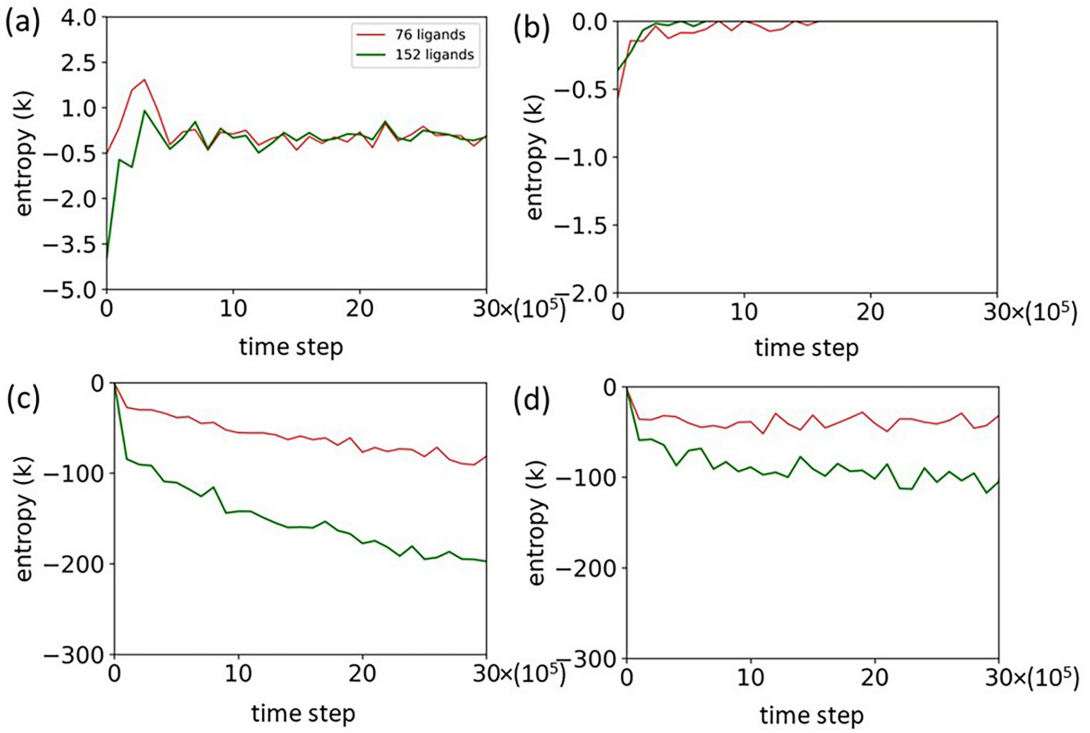

FIG. 5. Time evolution of (a) EG entropy, (b) ligand-1 entropy, (c) ligand-2 entropy, and (d) shell entropy of $8R_c$ Janus rod with different ligand densities. The red (thin) and green (thick) curves indicate Janus NC with 76 and 152 ligands, respetively.

chains, thereby constraining the freedom of motion for the EG chains.

As observed in Fig. S2 [76], both high and low ligand densities of Janus NCs lead to lower EG entropy loss (i.e., more disordered EG chains) compared to unembedded EG. Due to the stronger attractive interaction between ligand 1 and EG chains, all ligand densities of Janus NCs facilitate increased freedom of movement for the EG chains. Overall, the EG entropy loss plays a crucial role as a driving force for the penetration of Janus rods with low ligand density.

Furthermore, Janus NCs with higher ligand density exhibit lower ligand-1 entropy loss [Fig. 5(b)]. The presence of more ligand 1 at the EG/water interface results in a highly attractive interaction, offering ligand-1 chains greater freedom to move. Consequently, at this ligand density, the Janus NC has more disordered ligand-1 chains. Thus, ligand-1 entropy loss acts as a delicate barrier for the penetration of high-ligand-density Janus rods.

Moreover, Janus NCs with higher ligand density experience a larger entropy loss of ligand 2 [Fig. 5(c)]. The high-ligand-density Janus NC encounters greater repulsion of EG and ligand 2, resulting in more ordered ligand-2 chains.

For Janus NCs with high ligand density, the shell exhibits greater orderliness [Fig. 5(d)] compared to low-ligand-density Janus NCs. The higher repulsion of EG and ligand 2 on the former Janus NC leads to a larger entropy loss in the shell for its ligand-2 functionalized hemisphere. As expected, the influence of penetration on the ligand-2 entropy loss is also reflected in the shell entropy loss.

In general, increasing the ligand density enhances both the driving force, such as potential energy, and barriers to Janus penetration, such as EG chains, ligand-2, and shell entropy losses. Thus, the proper ligand density is the one that results in more driving forces than barriers.

A Monte Carlo simulation conducted by Liu *et al.* [69] demonstrated that an expansion in ligand density of NCs enhances their targeting to endothelial cells, which aligns with our observations regarding Janus NCs.

In the context of this study, an elevation in ligand density was found to correlate with an increase in penetration depth. However, it is important to conduct additional investigations across various ligand densities to find scenarios where the escalation in ligand density helps the barriers surpass the driving forces.

C. Effect of shape

The simulation of NC inclusion into the PB has primarily focused on spherical NCs [37,78–80]. However, the specific functions required for various applications call for different shapes of NCs, which have been extensively studied for their potential in biological applications [44,45]. One simulation study involving NCs with different shapes found that, compared to spherical NCs, the penetration of anisotropic NCs into a PB is more challenging [39]. Therefore, in our study, it is crucial to understand how the geometry of NCs can influence their penetration into the EG layer. Figures 6 and 7 present the Z_MSD, potential energy, and entropy of the system as a function of NC shape.

The Z_MSD plot [Fig. 6(d)] and the potential energy plot [Fig. 6(e)] indicate that, despite having the same ligand density, each of the three shapes of Janus NC exhibits a different initial driving force for penetration.

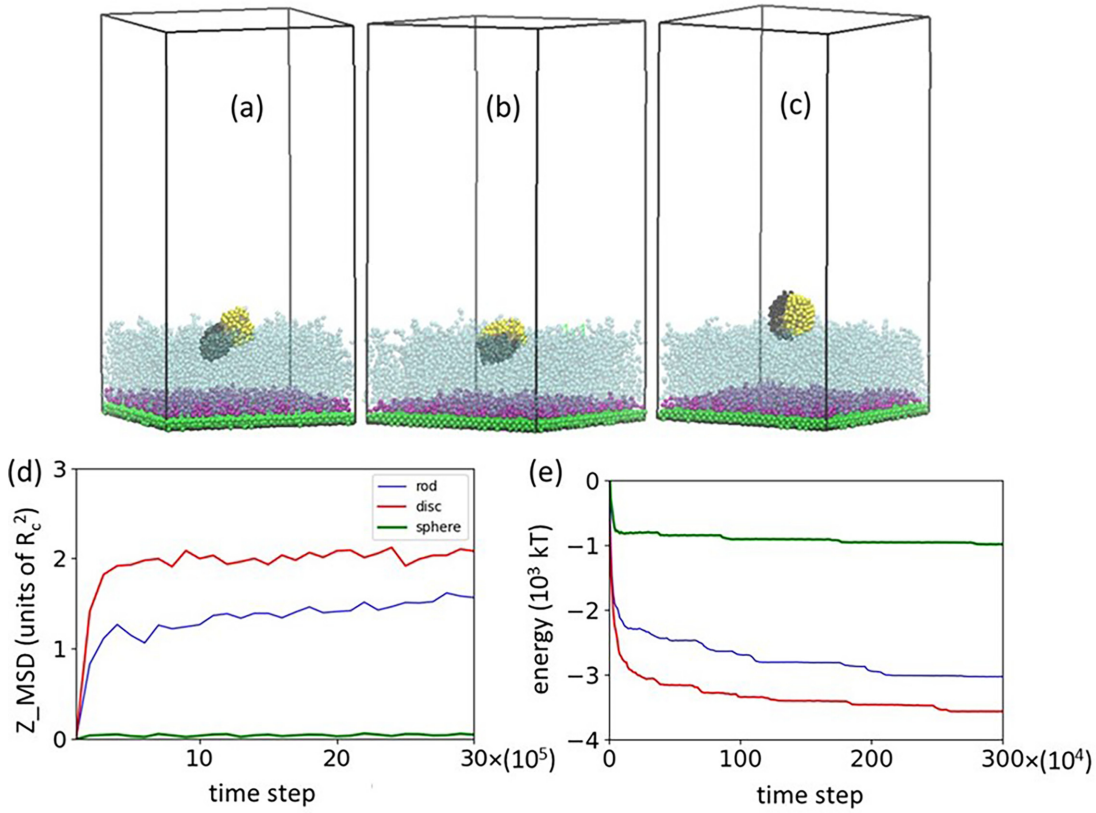

FIG. 6. VMD snapshots of (a) rod, (b) disk, and (c) sphere of $8R_c$ Janus NC after 30×10^5 time steps. (d) Z_MSD and (e) potential energy for these NCs with different shapes.

Disks, with the largest surface area in contact with EG chains compared to rods and spheres, have the highest attractive interaction with EG, resulting in the lowest potential energy. On the other hand, spheres, with the smallest surface area at the EG/water interface, have the lowest attractive interaction and thus show the highest potential energy. As time progresses, disks and rods experience a reduction in potential energy during penetration into the EG layer, with a higher number of ligand 1 in contact with EG chains, leading to greater attractive interactions. In contrast, spheres are unable to penetrate into the EG layer, resulting in no drop in potential energy over time. In summary, the shape with the elevated driving force exhibits deeper penetration. Therefore, for different Janus shapes, the potential energy difference determines the penetration amount.

Furthermore, for the disk-shaped NCs the EG entropy loss [Fig. 7(a)] is lower, indicating more disordered EG chains. As shown in Fig. S3 [76], the entropy loss of EG embedded with all shapes of Janus NC is more disordered than the entropy loss of EG without NCs. The attractive interaction between ligand 1 and EG chains in all shapes of Janus NCs allows for increased freedom of movement for EG chains during penetration.

Conversely, the Janus NC with a disk shape exhibits a distinctive characteristic. Despite its notable attraction to EG chains, resulting in the highest penetration depth, the penetration of the disk into the EG chains does not make them more ordered. Overall, the EG entropy loss serves as a strong driving force for the penetration of Janus disks.

For spheres, a high percentage of ligand 1 is located in contact with water, resulting in lower attractive interactions. As a consequence, the entropy loss of ligand 1 over time [Fig. 7(b)] is substantial, leading to more ordered ligand-1 chains. In contrast, the disks and rods experience highly attractive interactions of EG and ligand 1, offering ligand-1 chains more freedom to move. Thus, at these shapes, Janus NCs exhibit more disordered ligand-1 chains, leading to fewer barriers for penetration. As mentioned before, the disk also results in disordered EG chains. This suggests that the attractive interaction of EG and ligand 1 contributes to increased disorder in both EG chains and ligand-1 chains. Compared to other shapes, the ligand-1 entropy loss acts as a weaker barrier for the penetration of Janus disks.

The ligand-2 entropy loss [Fig. 7(c)] is higher for the disk shape, resulting in more ordered ligand-2 chains. As expected, the disk with the highest attractive interaction of EG and ligand 1 experiences the highest repulsion of EG and ligand 2, leading to the most ordered ligand-2 chains. Conversely, the sphere, with the least attractive potential energy, exhibits the most disordered ligand-2 chains.

Comparing to other shapes, the rod's shell becomes the most ordered [Fig. 7(d)]. It was anticipated that the disk, with a higher repulsion force on ligand 2, would cause a larger entropy loss of the shell. However, the rod, with a less repulsive interaction, shows the most entropy loss in its shell. One possible explanation is that the disk, with higher structural strength, undergoes less deformation than the rod. Consequently, the structural strength of the NC's shell can

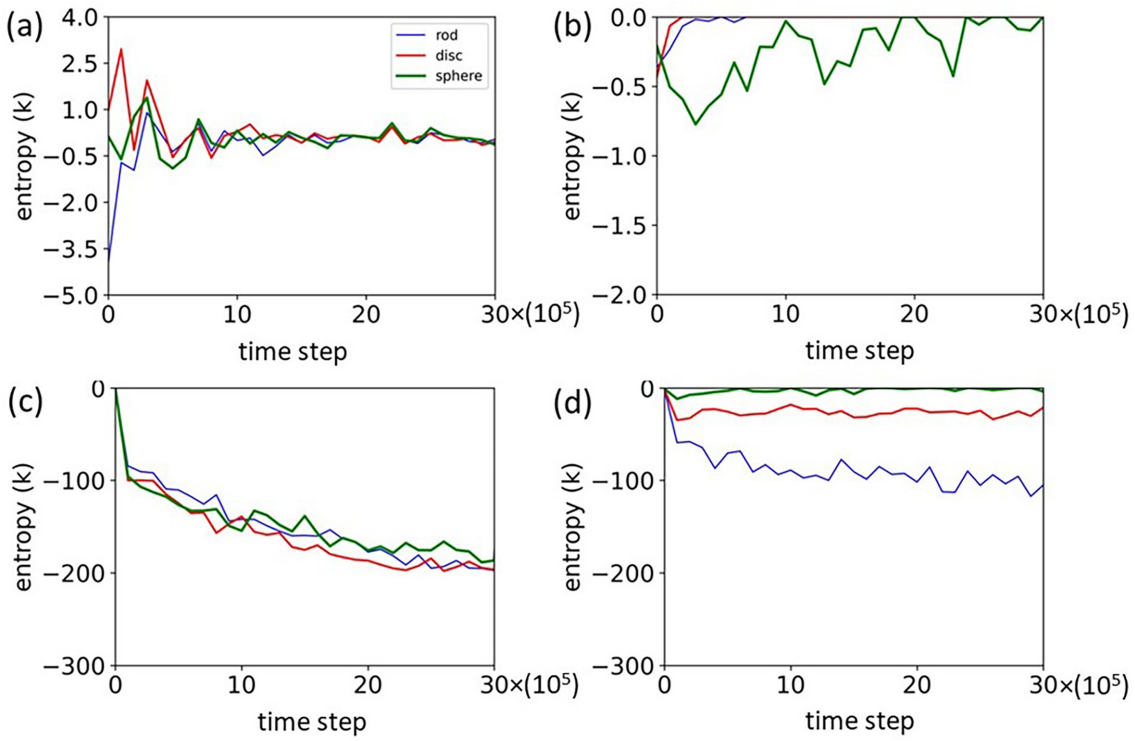

FIG. 7. Time evolution of (a) EG entropy, (b) ligand-1 entropy, (c) ligand-2 entropy, and (d) shell entropy of $8R_c$ Janus NC with different shapes. The blue, red, and green (from the thinnest to the thickest) curves indicate rod-, disk-, and sphere-shape Janus NCs, respectively.

control the shell entropy loss. As explained earlier, a Janus NC with a parallel orientation can rotate around the distinction line of ligand 1 and ligand 2 on its surface to penetrate inside the EG. The attraction of EG and ligand 1 and the repulsion of EG and ligand 2 act as two opposite forces on two hemispheres of the Janus NC, supporting its rotation. For a structurally strong shape of Janus NC like the sphere, these rotations over time do not significantly increase the shell's entropy loss. However, for structurally weak shapes like rods, these forces cause a bending of the rod at the distinction line, leading to a substantial rise in the shell's entropy loss. The penetration of the disk, with a moderate structural strength, results in a smaller shell entropy loss. As a result, the attractive force on ligand 1 can push the disk inside EG chains more effectively than the rod, which has less structural stiffness, providing further support for the better penetration of the disk.

In general, although the sphere has the lowest barriers, such as ligand-1 and shell entropy losses, the disk has the highest driving forces, such as the lowest potential energy and the lowest EG entropy loss, and thus penetrates better. In summary, driving forces control the penetration in different shapes. The superior penetration of the disk, with the largest surface area at the EG/water interface, aligns with the observations of Champion *et al.* [81], who studied the shape effect experimentally. They found that the surface area available for ligand adhesion from different shapes of NCs influences ligand adsorption and the amount of NC penetration.

Furthermore, studies by Sadhu *et al.* [82], Champion and Mitragotri [77], and Sharma *et al.* [83] delved into the engulfment of NCs with varying shapes. Their observations indicated that deviations from a spherical shape led to increased engulfment times. Our findings align with and support their observed trend.

D. Effect of size

Gao *et al.* [39] conducted a study on the effect of size on the inclusion energy of NCs into a PB and demonstrated that the osmotic pressure of the polymer brush layer determines the inclusion energy of the NC. In Figs. 8 and 9, the Z_MSD, potential energy, and entropy of the system are plotted as a function of NC diameters to characterize how the size of NCs can affect their penetration into the EG layer. According to the Z_MSD plot [Fig. 8(d)] and the potential energy plot [Fig. 8(e)], the initial potential energy indicates that the larger Janus NC, with a greater number of ligands, experiences a larger attractive interaction between EG and ligand 1, resulting in a lower potential energy. Changes in potential energy over time demonstrate that the penetration of the larger Janus NC leads to a greater exhausting of ligands through interactions with EG chains, resulting in less potential energy. For $8R_c$ and $12R_c$ Janus NCs, the trend of Z_MSD aligns with the trend of potential energy, where the $12R_c$ Janus NC, with a higher driving force, can penetrate more than the $8R_c$ Janus NC. Hence, the potential energy largely determines the penetration amount. However, the $16R_c$ Janus NC, despite having the highest driving force, cannot overcome the barriers, resulting in the lowest penetration among the different sizes of Janus NC.

Upon investigating the entropy losses during penetration, it is observed that, despite the increased attractive interaction between larger NCs and EG chains, their penetration leads to more ordered EG chains compared to the penetration of

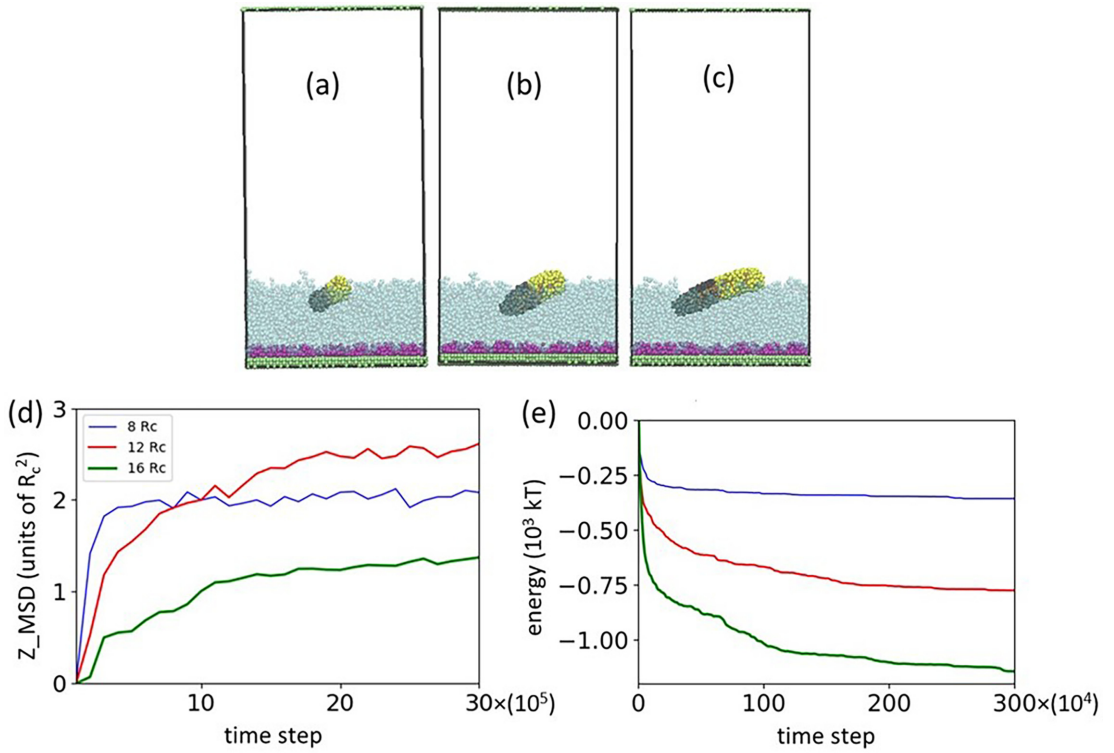

FIG. 8. VMD snapshots of (a) $8r_c$, (b) $12r_c$, and (c) $16r_c$ of disk-shaped Janus NC after 30×10^5 time steps. (d) Z_MSD and (e) potential energy for these NCs with different sizes.

smaller NCs [Fig. 9(a)]. This event is attributed to the fact that the penetration of larger NCs occupies more space between EG chains, therefore constraining the freedom of motion for the EG chains.

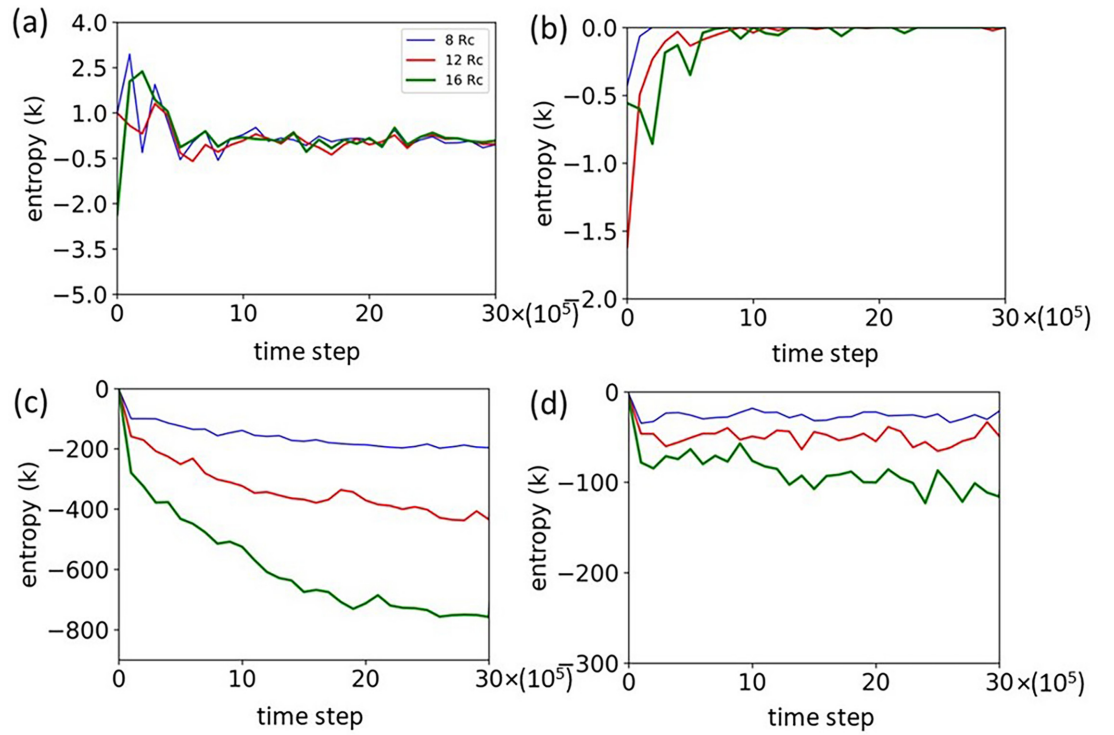

FIG. 9. Time evolution of (a) EG entropy, (b) ligand-1 entropy, (c) ligand-2 entropy, and (d) shell entropy of disk-shaped Janus NC with different sizes. The blue, red, and green (from the thinnest to the thickest) curves indicate $8R_c$, $12R_c$, and $16R_c$ Janus NCs, respectively.

As shown in Fig. S4 [76], for all sizes of Janus NC, the EG chains are more disordered than the unembedded EG chains. The attractive interaction of all Janus NCs with the EG layer allows for more freedom of movement for the EG chains.

In conclusion, for larger sizes of Janus NC, in addition to the attraction between EG and ligand 1, size-induced restriction on the conformation of EG chains can control the EG entropy loss [39]. Comparatively, for smaller Janus disks, the EG entropy loss becomes a strong driving force for their penetration.

Figure 9(b) illustrates that for the larger Janus NC with more attractive potential energy, despite the expected increase in disorder of ligand-1 chains, there is a greater ligand-1 entropy loss. As mentioned earlier regarding the EG entropy loss, larger NCs occupy more space between EG chains, resulting in increased ordering of EG chains. Additionally, there is a direct relationship observed between the entropies of EG chains and ligand 1. Larger NCs experience a larger entropy loss of EG chains, which also leads to a larger entropy loss of ligand-1 chains.

As time passes and ligand 1 penetrates into the EG layer, there is no longer any contact between water and ligand 1, causing the entropy of the latter to reduce to zero. The faster ligand 1 penetrates into the EG layer, the steeper the slope of decrease in the entropy loss of ligand 1. In summary, the ligand-1 entropy loss serves as a weak barrier for the penetration of smaller size disks.

Similarly, the ligand-2 entropy [Fig. 9(c)] is also greater for larger Janus NCs, as expected. Larger size NCs with higher attractive interaction of EG and ligand 1 also exhibit higher repulsion of EG and ligand 2, resulting in more ordered ligand-2 chains.

Furthermore, for the larger size of Janus NC, the shell becomes more ordered [Fig. 9(d)] compared to the smaller size of Janus NCs. In the case of larger disks, the higher repulsion force on the ligand-2 side causes a larger entropy loss of the shell for the ligand-2 functionalized hemisphere of the Janus NC. In other words, the increase in the ligand-2 entropy loss directly contributes to the overall increase in the shell entropy loss of the Janus NC. One possible explanation for the high shell entropy loss of the $16R_c$ Janus NC is that the two forces acting on the hydrophilic and hydrophobic hemispheres cause bending of the large disk at the distinction line, and this significant deformation can be a barrier for the slower diffusion of larger Janus NCs.

Although the $16R_c$ Janus NC has the highest driving force for the penetration, such as the lowest potential energy, its barriers, such as EG chains, ligand 1, ligand 2, and shell entropy losses, are significantly high, thus resulting in the slowest dynamics. On the other hand, at this grafting density, the $12R_c$ Janus NC has enough driving force and a strong structure that it can rotate around the distinction line and penetrate well into the EG layer.

Overall, for different sizes of NCs, barriers play a key role in controlling the penetration process. Gao *et al.* [39] discovered that the penetration free energy is affected more by the increase in the size of NCs. Their results support our observation about the effect of size, which induces more entropy losses than attractive potential energies, resulting in NCs penetrating in lower amounts.

Also Sadhu *et al.* [82] explored the engulfment of NCs with varying sizes. Their findings revealed that extremely small particles face challenges in internalization due to high bending energy of the vesicles, whereas excessively large particles necessitate larger vesicles for complete internalization. In our system, the $8R_c$ Janus NC, similar to the findings in their study, encounters limitations in deep penetration due to a relatively low attractive interaction with the EG layer. Conversely, the $16R_c$ Janus NC penetrates less than others, which is primarily attributed to the substantial initial entropy loss of the EG chains during its penetration.

In general, the penetration amount of Janus NCs is influenced by the interplay of various properties. Each individual property has its distinct impact on the penetration process, and, when combined, these properties can collectively affect the overall penetration amount. In other words, a Janus NC with a variety of properties has a unique combination of driving forces and barriers for penetration. By changing the assortment of properties, the combination of driving forces and barriers can be altered, leading to changes in the penetration depth. For instance, the $8R_c$ Janus rod with high ligand density can penetrate inside the EG layer, whereas the sphere shape or $16R_c$ size Janus NC, with their high ligand density, have lower penetration depths compared to other shapes or smaller sizes, respectively.

Finally, it should be noted that the repulsion parameters used in this coarse-grained simulation are chosen to cover all interaction types in the process of adhesion and penetration of Janus NCs to endothelial cells. However, there is a significant need for a multiscale simulation of this system to accurately determine the repulsion parameters of the protein constituents comprising the receptors, EG chains, and ligands. These parameters can be extracted from an atomistic molecular dynamics simulation and applied to this coarse-grained DPD simulation of NCs targeting endothelial cells. Such a multiscale approach would enhance the accuracy and reliability of the simulation results and provide deeper insights into the penetration process of Janus NCs.

IV. CONCLUSIONS

In this study, the adhesion and penetration process of Janus NCs with varying initial orientations, ligand densities, shapes, and sizes to endothelial cells is thoroughly investigated. The role of potential energy and entropy in relation to several parameters, such as the characteristics of the endothelial cell layer, the presence of hydrophilic and hydrophobic ligands, and the properties of the NC shell, is explored. Regarding the effect of initial orientation, it is observed that when Janus NCs aligned their long axis in parallel with the EG layer, the resulting low potential energy and minimal shell entropy loss facilitated a substantial penetration of Janus NCs into the cell layer. Moving on to the ligand density effect, it is found that Janus NCs with higher ligand density exhibited increased ligand-1 and ligand-2 entropies. Despite this, the higher potential energy associated with higher ligand density allowed the NC to overcome entropic penalties, resulting in faster dynamics. As ligand density increased, both driving forces and barriers also rose. However, for specific Janus NCs with an optimal ligand density, the

driving forces prevailed over the barriers, facilitating penetration into the endothelial cell layer. The shape effect suggests that, initially, the disk shape has the highest driving force for penetration due to its larger surface area in contact with the EG layer. On the other hand, the rod and the sphere shapes have higher barriers, resulting in a less favorable penetration. The weaker structural strength of certain shapes leads to higher shell entropy loss, creating more barriers to penetration. Both potential energy and shell entropy loss play a role in controlling the penetration of Janus NCs for different shapes. Regarding the size effect, it indicates that there exists a threshold size for Janus NCs at a certain ligand density. Janus NCs larger than this threshold size face higher barriers that hinder effective penetration. To improve penetration for larger Janus NCs, the ligand density can be increased or the structural strength of the NC can be enhanced. By fine-tuning the size and stiffness of Janus NCs at a specific ligand density, barriers can be reduced, enhancing the adsorption of Janus NCs to the cell. The increase in ligand density amplifies both driving forces and barriers for penetration, making it crucial to find the proper ligand density that enables driving forces to surpass barriers.

In conclusion, the shell entropy loss of Janus NCs is a dominant factor in determining the effects of initial orientation, shape, and size on their penetration. For the size and ligand density effects, the ligand-2 entropy loss controls the shell entropy loss, while for the shape and orientation effects, the structural strength of the shape or orientation plays a role in determining the shell entropy loss. Notably, the shell entropy loss caused by the structural strength is significantly higher than the shell entropy loss influenced by the ligand-2 entropy loss.

ACKNOWLEDGMENTS

This work was supported by the NSF, Grant No. CBET 1703919.

There are no conflicts to declare.

[1] S. Shukla, F. J. Eber, A. S. Nagarajan, N. A. Difranco, N. Schmidt, A. M. Wen, S. Eiben, R. M. Twyman, C. Wege, and N. F. Steinmetz, The impact of aspect ratio on the biodistribution and tumor homing of rigid soft-matter nanorods, Adv. Healthcare Mater. **4**, 874 (2015).

[2] S. Shukla, A. M. Wen, N. R. Ayat, U. Commandeur, R. Gopalkrishnan, A.-M. Broome, K. W. Lozada, R. A. Keri, and N. F. Steinmetz, Biodistribution and clearance of a filamentous plant virus in healthy and tumor-bearing mice, Nanomedicine **9**, 221 (2014).

[3] A. M. Wen, P. H. Rambhia, R. H. French, and N. F. Steinmetz, Design rules for nanomedical engineering: From physical virology to the applications of virus-based materials in medicine, J. Biol. Phys. **39**, 301 (2013).

[4] A. M. Wen, and N. F. Steinmetz, The aspect ratio of nanoparticle assemblies and the spatial arrangement of ligands can be optimized to enhance the targeting of cancer cells, Adv. Healthcare Mater. **3**, 1739 (2014).

[5] D. R. Elias, A. Poloukhtine, V. Popik, and A. Tsourkas, Effect of ligand density, receptor density, and nanoparticle size on cell targeting, Nanomedicine (N.Y., NY, U.S.) **9**, 194 (2013).

[6] M. Ghezzi, S. Pescina, C. Padula, P. Santi, E. Del Favero, L. Cantù, and S. Nicoli, Polymeric micelles in drug delivery: An insight of the techniques for their characterization and assessment in biorelevant conditions, J. Controlled Release **332**, 312 (2021).

[7] H. S. Sakhalkar, M. K. Dalal, A. K. Salem, R. Ansari, J. Fu, M. F. Kiani, D. T. Kurjiaka, J. Hanes, K. M. Shakesheff, and D. J. Goetz, Leukocyte-inspired biodegradable particles that selectively and avidly adhere to inflamed endothelium in vitro and in vivo, Proc. Natl. Acad. Sci. USA **100**, 15895 (2003).

[8] N. J. Agrawal and R. Radhakrishnan, The role of glycocalyx in nanocarrier-cell adhesion investigated using a thermodynamic model and Monte Carlo simulations, J. Phys. Chem. C **111**, 15848 (2007).

[9] S. Sabri, Glycocalyx modulation is a physiological means of regulating cell adhesion, J. Cell Sci. **113**, 1589 (2000).

[10] A. Kabedev and V. Lobaskin, Structure and elasticity of bush and brush-like models of the endothelial glycocalyx, Sci. Rep. **8**, 240 (2018).

[11] Y. Wang, Z. Li, J. Xu, C. Yang, and G. E. Karniadakis, Concurrent coupling of atomistic simulation and mesoscopic hydrodynamics for flows over soft multi-functional surfaces, Soft Matter **15**, 1747 (2019).

[12] D. R. M. Williams and P. A. Pincus, Polymer brushes: A hydrodynamic analogy, Europhys. Lett. **24**, 29 (1993).

[13] J. U. Kim and B. O'Shaughnessy, Nanoinclusions in dry polymer brushes, Macromolecules **39**, 413 (2006).

[14] A. Daddi-Moussa-Ider, S. Goh, B. Liebchen, C. Hoell, A. J. T. M. Mathijssen, F. Guzmán-Lastra, C. Scholz, A. M. Menzel, and H. Löwen, Membrane penetration and trapping of an active particle, J. Chem. Phys. **150**, 064906 (2019).

[15] A. Halperin, M. Kröger, and E. B. Zhulina, Colloid-brush interactions: The effect of solvent quality, Macromolecules **44**, 3622 (2011).

[16] T. Lewis and V. Ganesan, Interactions between grafted cationic dendrimers and anionic bilayer membranes, J. Phys. Chem. B **117**, 9806 (2013).

[17] M. Surve, V. Pryamitsyn, and V. Ganesan, Polymer-bridged gels of nanoparticles in solutions of adsorbing polymers, J. Chem. Phys. **125**, 064903 (2006).

[18] K. Chen and Y. Q. Ma, Interactions between colloidal particles induced by polymer brushes grafted onto the substrate, J. Phys. Chem. B **109**, 17617 (2005).

[19] S. A. Egorov and K. Binder, Effect of solvent quality on the dispersibility of polymer-grafted spherical nanoparticles in polymer solutions, J. Chem. Phys. **137**, 094901 (2012).

[20] J. U. Kim and M. W. Matsen, Repulsion exerted on a spherical particle by a polymer brush, Macromolecules **41**, 246 (2008).

[21] M. Murat and G. S. Grest, Molecular dynamics simulations of the force between a polymer brush and an AFM tip, Macromolecules **29**, 8282 (1996).

[22] H. Merlitz, C. X. Wu, and J. U. Sommer, Inclusion free energy of nanoparticles in polymer brushes, Macromolecules **45**, 8494 (2012).
[23] T. Curk, F. J. Martinez-Veracoechea, D. Frenkel, and J. Dobnikar, Collective ordering of colloids in grafted polymer layers, Soft Matter **9**, 5565 (2013).
[24] D. Romeis and J. U. Sommer, Conformational switching of modified guest chains in polymer brushes, J. Chem. Phys. **139**, 044910 (2013).
[25] G. G. Vogiatzis and D. N. Theodorou, Structure of polymer layers grafted to nanoparticles in silica-polystyrene nanocomposites, Macromolecules **46**, 4670 (2013).
[26] Q. Zhang and X. Xiang, Adsorption of a spherical nanoparticle in polymer brushes: Brownian dynamics investigation, Phys. A Stat. Mech. Appl. **392**, 3857 (2013).
[27] O. A. Guskova, S. Pal, and C. Seidel, Organization of nanoparticles at the polymer brush-solvent interface, Europhys. Lett. **88**, 38006 (2009).
[28] Y. Gong, X. Ma, K. H. Luo, H. Xu, and S. Shuai, A molecular dynamics study of evaporation mode transition of hydrocarbon fuels under supercritical conditions, Combust. Flame **246**, 112397 (2022).
[29] J. Cheng, A. Vishnyakov, and A. V. Neimark, Adhesion of nanoparticles to polymer brushes studied with the ghost tweezers method, J. Chem. Phys. **142**, 034705 (2015).
[30] G. M. Torrie and J. P. Valleau, Nonphysical sampling distributions in Monte Carlo free-energy estimation: Umbrella sampling, J. Comput. Phys. **23**, 187 (1977).
[31] S. De Beer, L. I. S. Mensink, and B. D. Kieviet, Geometry-dependent insertion forces on particles in swollen polymer brushes, Macromolecules **49**, 1070 (2016).
[32] Y. Li, M. Kröger, and W. K. Liu, Shape effect in cellular uptake of pegylated nanoparticles: Comparison between sphere, rod, cube and disk, Nanoscale **7**, 16631 (2015).
[33] Y. Li, M. Kröger, and W. K. Liu, Endocytosis of pegylated nanoparticles accompanied by structural and free energy changes of the grafted polyethylene glycol, Biomaterials **35**, 8467 (2014).
[34] K. Namdee, A. J. Thompson, P. Charoenphol, and O. Eniola-Adefeso, Margination propensity of vascular-targeted spheres from blood flow in a microfluidic model of human microvessels, Langmuir **29**, 2530 (2013).
[35] R. C. Van Lehn, P. U. Atukorale, R. P. Carney, Y. S. Yang, F. Stellacci, D. J. Irvine, and A. Alexander-Katz, Effect of particle diameter and surface composition on the spontaneous fusion of monolayer-protected gold nanoparticles with lipid bilayers, Nano Lett. **13**, 4060 (2013).
[36] A. Milchev, D. I. Dimitrov, and K. Binder, Excess free energy of nanoparticles in a polymer brush, Polymer **49**, 3611 (2008).
[37] M. G. Opferman, R. D. Coalson, D. Jasnow, and A. Zilman, Morphology of polymer brushes infiltrated by attractive nanoinclusions of various sizes, Langmuir **29**, 8584 (2013).
[38] T. Curk, F. J. Martinez-Veracoechea, D. Frenkel, and J. Dobnikar, Nanoparticle organization in sandwiched polymer brushes, Nano Lett. **14**, 2617 (2014).
[39] H. M. Gao, B. Li, R. Zhang, Z. Y. Sun, and Z. Y. Lu, Free energy for inclusion of nanoparticles in solvated polymer brushes from molecular dynamics simulations, J. Chem. Phys. **152**, 094905 (2020).
[40] K. Yang and Y. Q. Ma, Computer simulation of the translocation of nanoparticles with different shapes across a lipid bilayer, Nat. Nanotechnol. **5**, 579 (2010).
[41] K. Vahidkhah and P. Bagchi, Microparticle shape effects on margination, near-wall dynamics and adhesion in a three-dimensional simulation of red blood cell suspension, Soft Matter **11**, 2097 (2015).
[42] N. Doshi, B. Prabhakarpandian, A. Rea-Ramsey, K. Pant, S. Sundaram, and S. Mitragotri, Flow and adhesion of drug carriers in blood vessels depend on their shape: A study using model synthetic microvascular networks, J. Controlled Release **146**, 196 (2010).
[43] D. Zhang, J. Cheng, Y. Jiang, X. Wen, and L. Zhang, Orientation transition of nanorods induced by polymer brushes, J. Polym. Sci. Part B Polym. Phys. **51**, 392 (2013).
[44] G. Agrawal and R. Agrawal, Janus nanoparticles: Recent advances in their interfacial and biomedical applications, ACS Appl. Nano Mater. **2**, 1738 (2019).
[45] T. C. Le, J. Zhai, W.-H. Chiu, P. A. Tran, and N. Tran, Janus particles: Recent advances in the biomedical applications, Int. J. Nanomed. **14**, 6749 (2019).
[46] S. A. Shandiz, G. M. Leuty, H. Guo, A. H. Mokarizadeh, J. M. Maia, and M. Tsige, Structure and thermodynamics of linear, ring, and catenane polymers in solutions and at liquid–liquid interfaces, Langmuir **39**, 7154 (2023).
[47] S. Akbarishandiz, S. Khani, and J. Maia, Adhesion dynamics of functionalized nanocarriers to endothelial cells: A dissipative particle dynamics study, Soft Matter **19**, 9254 (2023).
[48] S. A. Akbarishandiz, S. Ray, F. Zhou, X. Chen, and J. Maia, Machine learning of performance space mapping for the DPD simulation of drug delivery to endothelial cells, Mol. Simul. **50**, 622 (2024).
[49] J. M. V. A. Koelman and P. J. Hoogerbrugge, Dynamic simulations of hard-sphere suspensions under steady shear, Europhys. Lett. **21**, 363 (1993).
[50] F. L. Paiva, A. R. Secchi, V. Calado, J. Maia, and S. Khani, Slip and momentum transfer mechanisms mediated by Janus rods at polymer interfaces, Soft Matter **16**, 6662 (2020).
[51] M. Jehser, G. Zifferer, and C. N. Likos, Scaling and interactions of linear and ring polymer brushes via DPD simulations, Polymers (Basel) **11**, 541 (2019).
[52] F. L. Paiva, M. J. A. Hore, A. Secchi, V. Calado, J. Maia, and S. Khani, Dynamic interfacial trapping of Janus nanorod aggregates, Langmuir **36**, 4184 (2020).
[53] S. Jamali, M. Yamanoi, and J. Maia, Bridging the gap between microstructure and macroscopic behavior of monodisperse and bimodal colloidal suspensions, Soft Matter **9**, 1506 (2013).
[54] S. Liu, S. Jamali, Q. Liu, J. Maia, J.-B. Baek, N. Jiang, M. Xu, and L. Dai, Conformational transitions of polymer brushes for reversibly switching graphene transistors, Macromolecules **49**, 7434 (2016).
[55] S. Khani, S. Jamali, A. Boromand, M. J. A. Hore, and J. Maia, Polymer-mediated nanorod self-assembly predicted by dissipative particle dynamics simulations, Soft Matter **11**, 6881 (2015).
[56] E. I. Barcelos, S. Khani, M. F. Naccache, and J. Maia, Supervised learning for accurate mesoscale simulations of suspension flow in wall-bounded geometries, Phys. Fluids **34**, 29 (2022).
[57] A. Boromand, S. Jamali, and J. M. Maia, Structural fingerprints of yielding mechanisms in attractive colloidal gels, Soft Matter **13**, 458 (2017).

[58] E. I. Barcelos, S. Khani, A. Boromand, L. F. Vieira, A. J. Lee, J. Peet, M. Naccache, and J. Maia, Controlling particle penetration and depletion at the wall using dissipative particle dynamics, Comput. Phys. Commun. **258**, 107618 (2020).

[59] Y. Kobayashi and N. Arai, Janus or homogeneous nanoparticle mediated self-assembly of polymer electrolyte fuel cell membranes, RSC Adv. **8**, 18568 (2018).

[60] R. D. Groot and P. B. Warren, Dissipative particle dynamics: Bridging the gap between atomistic and mesoscopic simulation, J. Chem. Phys. **107**, 4423 (1997).

[61] S. Biagi, L. Rovigatti, F. Sciortino, and C. Misbah, Surface wave excitations and backflow effect over dense polymer brushes, Sci. Rep. **6**, 22257 (2016).

[62] M. Deng, X. Li, H. Liang, B. Caswell, and G. E. Karniadakis, Simulation and modelling of slip flow over surfaces grafted with polymer brushes and glycocalyx fibres, J. Fluid Mech. **711**, 192 (2012).

[63] K. P. Santo, A. Vishnyakov, Y. Brun, and A. V. Neimark, Critical conditions of adhesion and separation of functionalized nanoparticles on polymer grafted substrates, J. Phys. Chem. C **123**, 16091 (2019).

[64] J. A. Millan, W. Jiang, M. Laradji, and Y. Wang, Pressure driven flow of polymer solutions in nanoscale slit pores pressure driven flow of polymer solutions in nanoscale slit pores., J. Chem. Phys. **126**, 124905 (2007).

[65] H. Wang, Y. T. Liu, H. J. Qian, and Z. Y. Lu, Dissipative particle dynamics simulation study on complex structure transitions of vesicles formed by comb-like block copolymers, Polymer **52**, 2094 (2011).

[66] B. M. Fu and J. M. Tarbell, Mechano-sensing and transduction by endothelial surface glycocalyx: Composition, structure, and function, Wiley Interdiscip. Rev. Mech. Dis. **5**, 381 (2013).

[67] E. C. Cho, L. Au, Q. Zhang, and Y. Xia, The effects of size, shape, and surface functional group of gold nanostructures on their adsorption and internalization by cells, Small **6**, 517 (2010).

[68] H. Chen, H. Paholak, M. Ito, K. Sansanaphongpricha, W. Qian, Y. Che, and D. Sun, "Living" PEGylation on gold nanoparticles to optimize cancer cell uptake by controlling targeting ligand and charge densities, Nanotechnology **24**, 355101 (2013).

[69] J. Liu, G. E. R. Weller, B. Zern, P. S. Ayyaswamy, D. M. Eckmann, V. R. Muzykantov, and R. Radhakrishnan, Computational model for nanocarrier binding to endothelium validated using in vivo, in vitro, and atomic force microscopy experiments, Proc. Natl. Acad. Sci. USA **107**, 16530 (2010).

[70] P. M. Piaggi and M. Parrinello, Entropy based fingerprint for local crystalline order, J. Chem. Phys. **147**, 114112 (2017).

[71] M. Hadi, N. Sefiddashti, B. J. Edwards, and B. Khomami, A thermodynamically inspired method for quantifying phase transitions in polymeric liquids with application to flow-induced crystallization of a polyethylene melt, Macromolecules **53**, 10487 (2020).

[72] M. Amini, K. Hasheminejad, and A. Montazeri, Experimentally guided MD simulation to enhance the shape memory behavior of polymer-based nanocomposites: Towards elaborating the underlying mechanism, Composites Part A **138**, 106055 (2020).

[73] I. Williams, F. Turci, J. E. Hallett, P. Crowther, C. Cammarota, G. Biroli, and C. P. Royall, Experimental determination of configurational entropy in a two-dimensional liquid under random pinning, J. Phys. Condens. Matter **30**, 094003 (2018).

[74] T. Morishita, Time-dependent principal component analysis: A unified approach to high-dimensional data reduction using adiabatic dynamics, J. Chem. Phys. **155**, 134114 (2021).

[75] S. A. Ghaffarizadeh and G. J. Wang, Excess entropy scaling in active-matter systems, J. Phys. Chem. Lett. **13**, 4949 (2022).

[76] See Supplemental Material at http://link.aps.org/supplemental/10.1103/PhysRevE.109.064408 for time evolution of EG entropies for the EG with NCs comparing to the EG without NCs.

[77] J. A. Champion and S. Mitragotri, Role of target geometry in phagocytosis, Proc. Natl. Acad. Sci. USA **103**, 4930 (2006).

[78] Y. Hua, D. Zhang, and L. Zhang, Compression-driven migration of nanoparticles in semiflexible polymer brushes, Polymer **83**, 67 (2016).

[79] F. Leónforte and M. Mü, Functional poly(n-isopropylacrylamide)/poly(acrylic acid) mixed brushes for controlled manipulation of nanoparticles, Macromolecules **49**, 5256 (2016).

[80] C.-W. Li, H. Merlitz, C.-X. Wu, and J.-U. Sommer, Nanopores as switchable gates for nanoparticles: A molecular dynamics study, Macromolecules **51**, 6238 (2018).

[81] J. A. Champion, Y. K. Katare, and S. Mitragotri, Particle shape: A new design parameter for micro- and nanoscale drug delivery carriers, J. Controlled Release **121**, 3 (2007).

[82] R. K. Sadhu, S. R. Barger, S. Penič, A. Iglič, M. Krendel, N. C. Gauthier, and N. S. Gov, A theoretical model of efficient phagocytosis driven by curved membrane proteins and active cytoskeleton forces, Soft Matter **19**, 31 (2022).

[83] G. Sharma, A. R. Sharma, S. S. Lee, M. Bhattacharya, J. S. Nam, and C. Chakraborty, Advances in nanocarriers enabled brain targeted drug delivery across blood brain barrier, Int. J. Pharm. (Amsterdam, Neth.) **559**, 360 (2019).